Electrochimica Acta 132 (2014) 251–257

Contents lists available at ScienceDirect

Electrochimica Acta

journal homepage: www.elsevier.com/locate/electacta

An Fe@Fe_3C-inserted carbon nanotube/graphite composite support providing highly dispersed Pt nanoparticles for ethanol oxidation

Rongfang Wang[a,*], Hui Wang[a], Hao Li[b], Wei Wang[a], Julian Key[c], Lindiwe Khotseng[c], Shan Ji[c,**]

[a] Key Laboratory of Eco-Environment-Related Polymer Materials, Ministry of Education of China, College of Chemistry and Chemical Engineering, Northwest Normal University, Lanzhou 730070, China
[b] Department of Chemical Engineering, Huizhou University, Huizhou, Guangdong 516007, China
[c] South African Institute for Advanced Materials Chemistry, University of the Western Cape, Cape Town 7535, South Africa

ARTICLE INFO

Article history:
Received 26 March 2014
Accepted 27 March 2014
Available online 4 April 2014

Keywords:
Iron/iron carbide
Carbon nanotube
Support
Plantinum
Ethanol oxiation ;

ABSTRACT

Iron/iron carbide-inserted carbon nanotube/graphite composite (Fe-C) was prepared by pyrolyzing a mixture of melamine and iron (III) chloride to form a support for high loading of Pt nanoparticles as a direct ethanol fuel cell anode catalyst. The obtained Fe-C was characterized by Raman spectroscopy, X-ray diffraction, transmission electron microscopy, and X-ray photoelectron spectroscopy. The Fe-C surface characteristics supported a high (40 wt%) loading of Pt nanoparticles with uniform dispersion and small particle size. Compared to Vulcan carbon-supported Pt (40 wt%), Fe-C-supported Pt exhibited enhanced catalytic activity for CO and ethanol oxidation, and high stability due to the effect of the Fe-C support material.

1. Introduction

Proton exchange membrane fuel cells (PEMFCs) directly convert chemical energy into electricity via electrochemical reactions occurring on the cathode and anode [1,2]. Currently, Pt or Pt-based catalysts are regarded as the best anode materials and are widely used in fuel cells [3–6]. However, the prohibitive cost, scarcity, and instability of Pt-based catalysts make them unsuitable for large-scale applications and thus hold back PEMFC commercialization [7,8]. Deposition of Pt and Pt-based alloys on a conductive carbon support can significantly reduce the cost and improve electrocatalytic performance. The interaction between the Pt or Pt alloy nanoparticles and the support improves electrocatalytic efficiency, reduces catalyst loss, assists in charges transfer, prevents catalyst poisoning, and improves the size distribution of catalyst particles [9–11]. Therefore, development of effective support materials for electrocatalysts shows promise for future PEMFC commercialization.

Highly conductive carbon blacks with high surface area, such as Vulcan XC-72, Shawinigan and black Pearl 2000, are commonly used as supports for Pt electrocatalysts [9]. However, despite the high surface area and good electrochemcial performance of carbon black, for practical applications, PEMFC anode catalysts still require better performance [11,12]. Recently, some merits of electrocatalysts, such as low Pt loading, high electrocatalytic activity, and good durability, have been achieved by using carbon supports doped with nitrogen, which create strong and effective interaction bewteen Pt nanoparticles and support [13–16]. Sun et al. reported that N-doped carbon nanotubes provide well dispersed Pt nanoparticles and prevent agglomeration of Pt on the support, thus enhance electrocatalytic activity of the catalysts [17]. Ma et al. have demonstrated that Pt deposited on N-doped carbon nanofibers forms smaller and more uniform sized nanoparticles that exhibit higher electrocatalytic acitivity towards methanol oxidation than Pt on deposited on non-doped carbon nanowires [18]. However, the synthesis procedures for N-doped carbon nanotubes and carbon nanofibers are complicated and the treatment may significantly deteriorate the preferred structure/morphology and thus decrease the carbon nanotube support effect [19].

In our previous work, we found that a N-containing carbon composite support with an oxide, such as SiO_2 [20,21], Fe_3O_4 [22,23], ZrO_2 [9], can significantly enhance the catalytic activity of electrocatalysts compared to Vulcan carbon; this results from the small

* Corresponding author. Tel.: +86 931 7971533; fax: +86 931 7971533.
** Corresponding author. Tel.: +27 21 9599316; fax: +27 21 9599316.
E-mail addresses: wrf38745779@126.com, wangrf@nwnu.edu.cn (R. Wang), sji@uwc.ac.za (S. Ji).

http://dx.doi.org/10.1016/j.electacta.2014.03.153
0013-4686/

particle size and/or the synergetic effect between the N atoms, metal particle, and the oxide. In the work of Sun et al. [24], a support composite with Sn-doped carbon nanotubes enhanced the catalytic activity of Pt nanoparticles compared to an ETEK Pt/C catalyst. Furthermore, Deng et al. [25] have reported that Fe inserted carbon nanotubes have high activity for oxygen reduction reaction owing to electron transfer from Fe particles to the carbon nanotubes, which results in decreased local work function on the carbon surface. Therefore, the effect of combining metal particles inserted into N-doped carbon nanotubes holds the possiblilty of combining previous advantageous features in a single support.

In this study, we synthesized a metal particle-inserted carbon nanotube support using an iron salt as catalyst during the pyrolysis of melamine. Iron, and/or iron carbide-inserted and N-doped carbon nanotubes were formed, along with the formation of graphite sheets. The composite was used as a support to disperse Pt nanopartcles with high metal loadings (i.e. 40 wt%). High and effective Pt loading is very important for PEMFC commercialization, which provides significant reductions in diffusion layer thickness, mass transport resistance, and fabrication cost of the supported Pt catalyst electrode [26,27]. The ethanol electrooxidation activity of the catalyst was evaluated and compared to that of a catalyst prepared on a conventional carbon black support.

2. Experimental

2.1. Preparation of catalyst

Iron nanoparticle-inserted carbon nanotube/graphite composite (Fe-C) was synthesized as follows: iron (III) chloride tetrahydrate (1.350 g) was dissolved in 40 ml ethanol with stirring, and 1.562 g melamine was added and stirred for 3 h. The suspension was vacuum-dried using a rotary evaporator, dried for 4 h at 60 °C, then heated at 800 °C for 1 h under nitrogen atomosphere in a tube furnace followed by heating in 0.5 mol L^{-1} H_2SO_4 at 80 °C for 8 h to remove unstable species. Finally, the sample was centrifuged, washed 10 times with ultrapure water, and the final product dried in vacuum oven at 60 °C for 4 h.

Pt/Fe-C was synthesized by a modified organic colloid method in an ethylene glycol (EG) solution as follows: 1.18 ml of H_2PtCl_6 (20 mg ml^{-1}) was dissolved in the solution containing 30 ml of EG and 35.3 mg of sodium citrate in a 100 ml flask. The solution was adjusted to pH 10 using 5 wt% of KOH/EG solution while stirring vigorously. Fe-C was introduced to the solution under ultrasonic condition, and the mixture was transferred to an autoclave and heated at 160 °C for 6 h. The resulting powder was collected by filtration, rinsed with ultrapure water several times, and dried in a vacuum oven at 60 °C for 6 h. Pt/Fe-C with 40 wt% metal loading was obtained. For comparison, the Pt/C (40 wt% Pt loading) with Vulcan XC-72 as a support was synthesized using the same method.

2.2. Characterization

X-ray diffraction (XRD) patterns were recorded on a Rigaku D/Max-2400 (Japan) diffractometer, using Cu Ka radiation operated at 40 kV and 30 mA. Raman spectroscopy was carried out on a Ft-Raman spectroscopy (RFS 100, BRU-KER) with Nd: YAG laser wavelength of 1064 nm. Transmission electron microscopy (TEM) measurements were carried out on a JEM-2010 Electron Microscope (Japan) with an acceleration voltage of 200 kV. X-ray photoelectron spectroscopy (XPS) was obtained using a VGEscalab210 spectrometer fitted with Mg 300 W X-ray source (England). The composition of the support was analyzed on an organic elemental analyzer (Thermo Flash 2000). The Pt loading of two samples were determined using an IRIS advantage inductively coupled plasma atomic emission spectroscopy (ICP-AES) system (Thermo, USA).

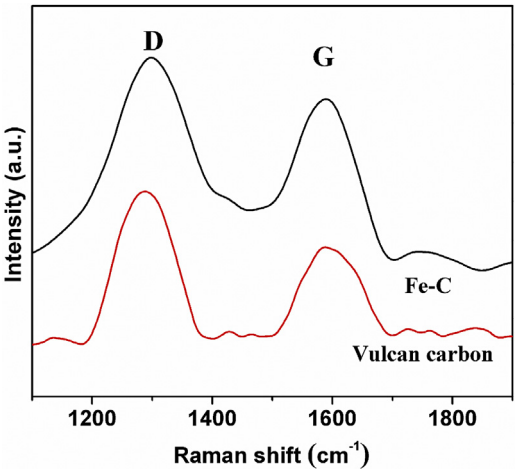

Fig. 1. Raman spectra of Fe-C and Vulcan carbon.

Electrochemical experiments were carried out using an Autolab electrochemical work station (CHI 650D). A conventional three-electrode cell was used for the electrochemical measurements, comprising an Ag/AgCl (3 mol L^{-1} KCl) reference electrode, a carbon rod as the counter electrode, and a modified glass carbon (5 mm in diameter) as the working electrode. The working electrode was prepared using 5 mg of catalyst dispersed ultrasonically in 1 ml of Nafion/ethanol (0.25% Nafion). About 8 μl of the dispersion was transferred onto the glassy carbon disc using a pipette, and then dried in the air to form catalyst layer on it. Before each measurement, the solution was purged with high-purity N_2 or O_2 gas for at least 30 min.

3. Results and Discussion

The Raman spectra of Fe-C and Vulcan carbon (Fig. 1) produced G and D peaks at around 1560 and 1300 cm^{-1}, respectively [28]. The D-band arises due to a reduction of symmetry near or at the crystalline edges, which is ascribed to the finite-sized crystals of graphite. The G-band is attributed to all sp^2 bonds of graphitic network [29]. The ratio of the relative intensities of D and G bands is indicative of the crystallinity of the carbon materials, i.e. the lower the I_D/I_G, the higher the crystallinity. By measuring the Raman spectra, the I_D/I_G of Fe-C and Vulcan carbon are 1.12 and 1.30, respectively. The I_D/I_G of Fe-C is lower than that of Vulcan carbon, which indicates that Fe-C has higher crystallinity than Vulcan carbon.

Fig. 2 shows TEM images of the synthesized Fe-C at different magnifications. It can be seen in Fig. 2a that the as-prepared carbon material is composed of carbon nanotubes and graphite fragments, ranging from about 5 nm to 150 nm. The formation of carbon nanotubes is due to the presence of Fe^{3+}, which provides a catalyst for carbon nanotube growth [29,30]. The coated particles contain Fe and/or Fe_3C (Fe@Fe_3C), which would be confirmed by the following XRD result. As shown in Fig. 2b, the shape of Fe-C nanotubes differs in having bamboo-like shape, curved shape, and twig-like shapes. The fine structure of graphite fragments is shown in Fig. 2c. The Fe@Fe_3C particle is completely coated by the graphite layers which cause the wrinkled and irregular curvature due to the propensity of incorporated nitrogen to form pentagonal and hexagonal defects in the graphite layers [12].

XPS analysis was used to investigate the elemental composition as well as the chemical bonding environment of Fe-C. From the survey scan of Fe-C shown in Fig. 3a, it can be seen that Fe-C

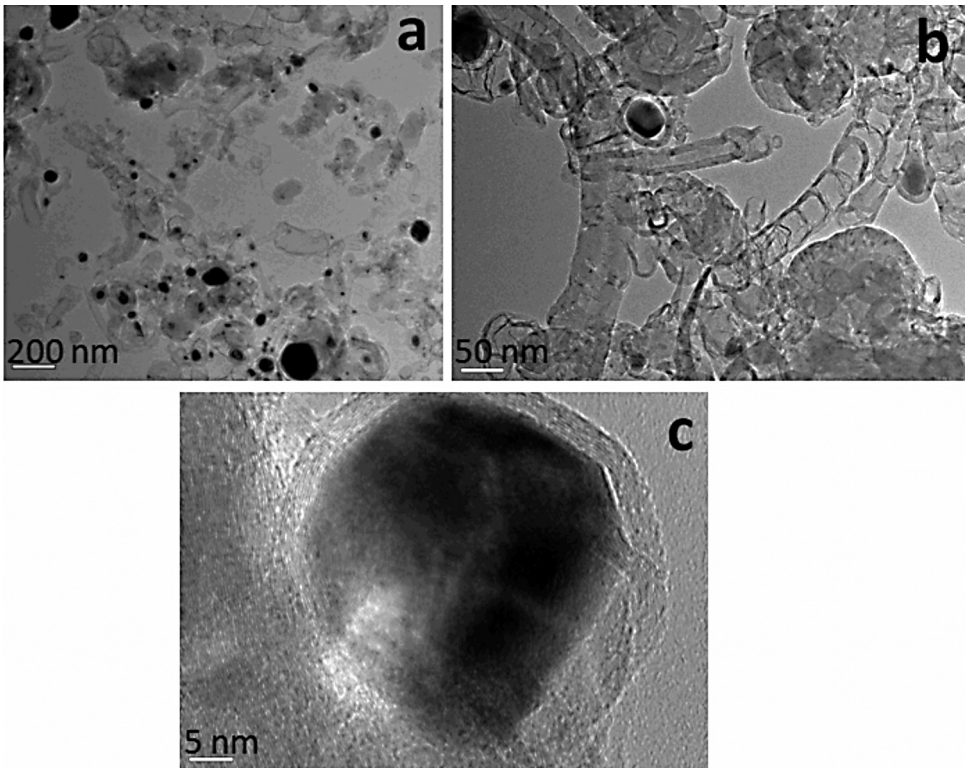

Fig. 2. TEM images with different magnifications of Fe-C.

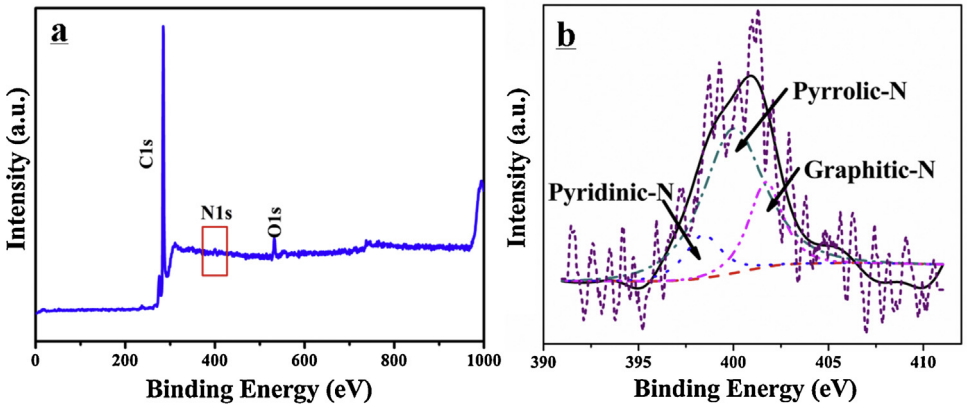

Fig. 3. (a) XPS survey spectrum and (b) N 1s spectrum of Fe-C.

contains N. It has been reported that carbon-based materials, such as coal and char, can contain four types of nitrogen species, namely pyridinic-N, pyrrolic-N, quaternary-N and pyridinic-N^--O^- [31]. As shown in Fig. 3b, there are three peaks in the N 1s spectrum of Fe-C. Pyridinic-N has a pair of electrons in the plane of the carbon matrix and provides one p electron to the aromatic π system, which is believed to be responsible for both the wall roughness and wrinkled morphology [12]. The relative amounts of the three types of N species are calculated from the corresponding fitted peaks, and the amount of each nitrogen species is tabulated in Table 1. The results show that pyridinic-N and pyrrolic-N are the dominant N species in the sample. These N atoms might provide the active sites for the dispersion of Pt nanoparticles. The content of N element in the bulk of Fe-C determined by an organic elemental analyzer is 3.1 wt%.

Fig. 4 shows the XRD pattern of Fe-C, Pt/Fe-C and Pt/C. In the case of Fe-C, the strong sharp peak (002) centered at $2\theta \approx 26.5^\circ$ indicates the crystalline nature of carbon nanotube [32]. The sharp

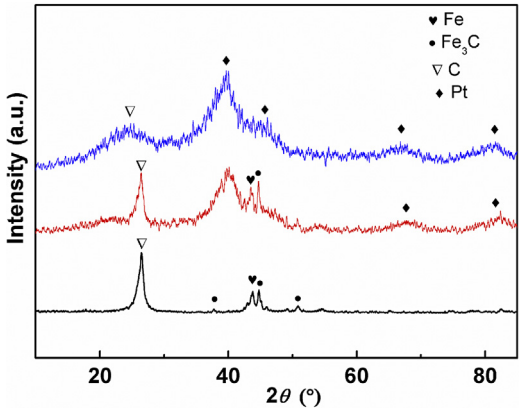

Fig. 4. XRD patterns of Pt/Fe-C and Pt/C.

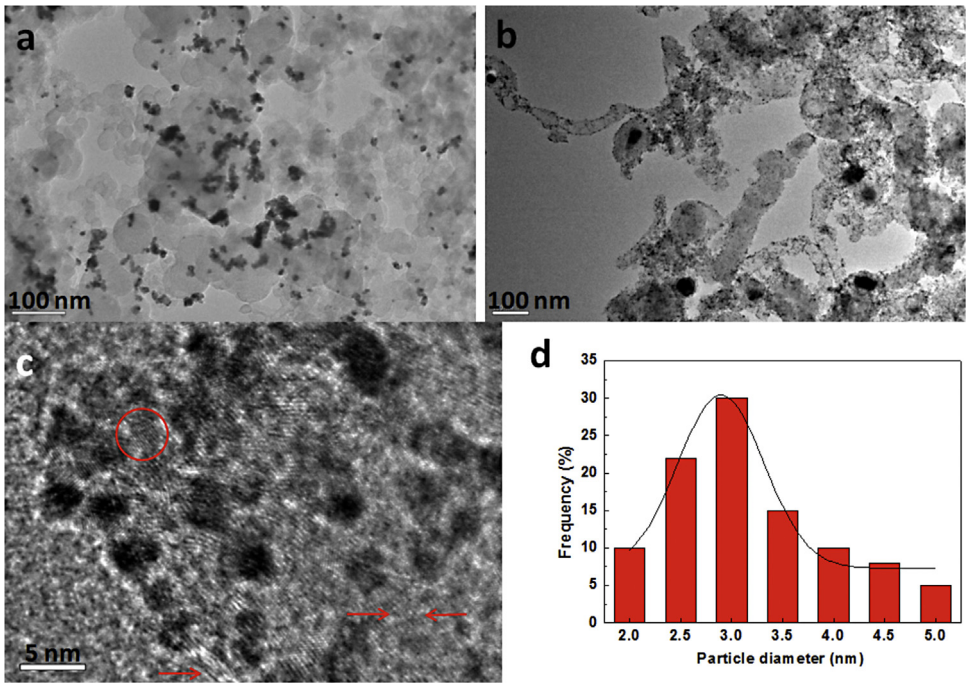

Fig. 5. TEM images of Pt/C (a) and Pt/Fe-C (b); HRTEM image of Pt/Fe-C (c), and the particle size distribution of Pt nanoparticles on Fe-C (d).

peaks at $2\theta \approx 44.5^\circ$ and 65.9° could be related to the reflection from (031) and (200) planes of Fe [33,34]. The two peaks located at 38.5 and 45.5° are ascribed to the (210) and (031) diffraction peaks of Fe_3C, and other weak peaks might also be assigned to the formation of Fe_3C [35]. These results indicate there are two species, e.g. Fe and Fe_3C, representing Fe element in the as-prepared carbon composite. The XRD pattern of Pt/C displays the four peaks at $2\theta \approx 40^\circ$, 46°, 68°, and 82°, corresponding to reflections from (111), (200), (220) and (311) planes of face centered cubic phase Pt [36]. In the case of Pt/Fe-C, besides the diffraction peaks of graphitic structure and α-Fe, three peaks related to the Pt (111), (220) and (311) planes appear, at $2\theta \approx 40^\circ$, 68° and 82°, where the Pt (200) plane is suppressed by the peaks of α-Fe. The XRD result implies that the synthesized Pt/Fe-C has similar crystalline structure to that of Pt/C. It should be noted that the crystallinity of Pt phase in the two catalysts does not look very good, apparently. The actual Pt loading measured by ICP is 39.7 wt% for Pt/Fe-C and 39.8 wt% for Pt/C, which are close to that in the precursors.

The TEM images of Pt/C and Pt/Fe-C are shown in Fig. 5. In Fig. 5a, Pt nanoparticles are dispersed on the surface of Vulcan carbon with significant aggregation. Generally, the degree of aggregation of nanosized electrocatalysts is associated with many factors, such as the surface of the support, the synthetic method of metal particles and the metal loading. In our previous work [37], Pt/C catalyst with the metal loading of 20 wt%, (prepared by a similar method to that in the present work) had uniform dispersion with little aggregation. Thus, the high loading in the present study caused aggregation of Pt on Pt/C. In contrast, the uniform dispersion of Pt nanoparticles on the surface of Fe-C (Fig. 5b) suggests Fe-C can provide more initial nucleation sites for anchoring small Pt nanoparticles avoiding coalescence of Pt at high metal loading. While, it can be observed that Pt particles shows spherical shape, and some spheres formed into short-wires. The high resolution TEM (HRTEM) image of Pt/Fe-C is shown in Fig. 5c. It can be seen that there are two phase; one is the Pt particles are confirmed by the contrast and the lattice plane such as the particle indicated by the red circle. The other is the Fe-C support indicated by the red arrows. As we seen, the Pt particles are mainly in spherical shape. The particle size distribution (Fig. 5d) ranges from ca. 2 to 5 nm with the mean particle size of ca. 3.0 nm. These results show that different supports affect the distribution of the metal nanoparticles.

The effect of the supports on chemical state of Pt was investigated by XPS (shown in Fig. 6). For the two catalysts, two peaks are observed at the Pt 4f binding energy attributed to $4f_{7/2}$ and $4f_{5/2}$ of Pt respectively. For Pt/Fe-C, the binding energies of $4f_{7/2}$ and $4f_{5/2}$ are 71.5 and 74.8 eV respectively, which are higher than that

Table 1
Binding energy and relative amounts of nitrogen species from curve-fitted XPS spectrum of Fe-C.

N-Species	N 1s Binding Energy (eV)	Peak Half Width (eV)	Relative Concentration (%)
Pyridinic-N	398.4	2.25	11.8
Pyrrolic-N	400.0	3.79	66.6
Graphitic-N	401.7	2.10	21.6

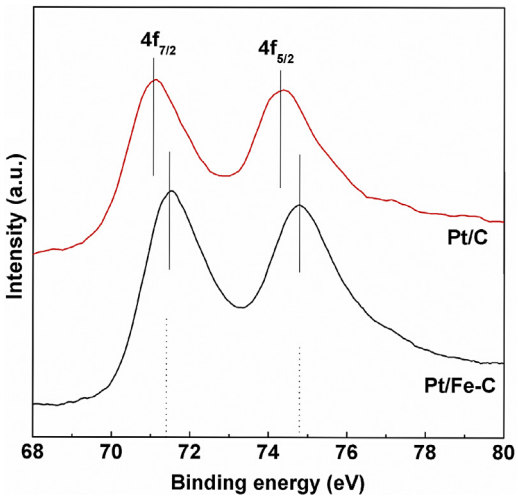

Fig. 6. Pt 4f XPS spectra of Pt/C and Pt/Fe-C.

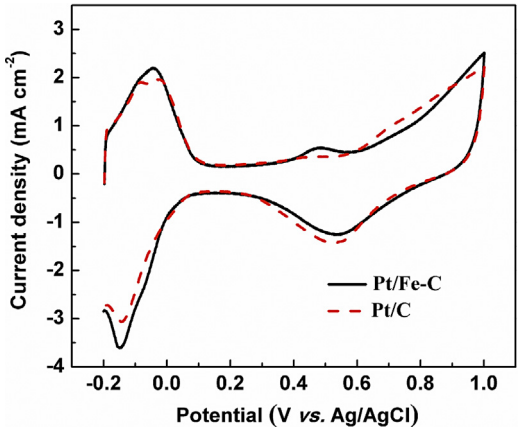

Fig. 7. Cyclic voltammograms of Pt/Fe-C and Pt/C catalysts in 0.5 mol L^{-1} H_2SO_4 solution saturated with N_2.

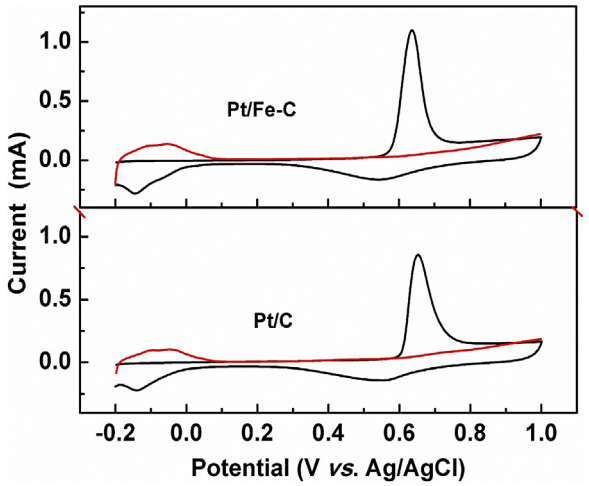

Fig. 8. CO stripping voltammograms for on Pt/Fe-C and Pt/C catalysts in 0.5 mol L^{-1} H_2SO_4 solution saturated with N_2.

of Pt/C at 71.1 and 74.3 eV. Compared to Pt/C, the positive shift in the binding energies of Pt/Fe-C is likely due to the following two factors. Firstly, the effect of small Pt nanoparticles deposited on a support cause a positive shift in the binding energy due to extra atomic relaxation effect [38,39]. Secondly, strong interaction between Pt nanoparticles and Fe-C can be inferred from previous literature on metal-doping and N-doping respectively [15,40]. So, which factor mainly influence the positive shift of Pt 4f XPS? If the Pt particles of Pt/Fe-C is obviously increased, how about the binding energy of Pt 4f XPS? Then, Pt/Fe-C were heat-treated at 300 °C for 3 h in order to obtain the aggregated Pt particles, which would have large size. As we expected, the aggregation occurs, which can be confirmed by TEM image (See Supporting Information). The Pt 4f binding energy of Pt/Fe-C with heat-treatment is shown as the vertical dot line in Fig. 6. It can be observed that the binding energies of Pt 4f XPS of Pt/Fe-C before heat-treatment is similar to that after heat-treatment, which is positive compared to that of Pt/C. The result implies that the positive shift in the Pt 4f binding energy of Pt/Fe-C is related to the strong interaction between Pt nanoparticles and Fe-C. The positive shift of binding energy of Pt implys that the d-band centre has a low energy value. The Pt surface with low d-band centre value tends to bind adsorbents such as CO more weakly, which would change the rate of ethanol oxidation [41,42].

The electrocatalytic activity of Pt/Fe-C was characterized by cyclic voltammetry (CV). Fig. 7 shows CVs of Pt/Fe-C measured in 0.5 M solution saturated with N_2 at room temperature. In the postive scan, both catalysts exhibit the characteristic features of polycrystalline Pt, i.e. examining the hydrogen desorption region ranged from -0.2 to 0.1 V, the double-layer region between 0.1 and 0.55 V, and the surface oxide (OH_{ads}) started at 0.55 V. Accordingly, in the backward scan, the surface oxide stripping peak around 0.53 V, the doule-layer region, and the absorption the hydrogen adsorption appear. In additon, in the case of Pt/Fe-C, a small oxidation peak at ca. 0.48 V appears, which relate to the oxidation of Fe species [23]. The electrochemical surface area (*ECSA*) of the catalysts was estimated from the integrated charge of the hydrogen adsorption/desorption region of the CV. The *ECSA* of Pt/Fe-C is 19.8 $m^2\ g^{-1}{}_{Pt}$, which is slightly larger than that of Pt/C (18.5 $m^2\ g^{-1}{}_{Pt}$), indicated that Pt/Fe-C provides more active sites for methanol oxidation.

The capability of a catalyst to oxidize chemisorbed CO is a key parameter of performance and is measured by CO stripping voltammograms. Fig. 8 shows the CO stripping voltammograms on Pt/Fe-C and Pt/C electrodes in N_2-staturated 0.5 mol L^{-1} H_2SO_4 solution at a scan rate of 50 mV s^{-1}. A peak current at ca. 0.65 V associated with CO oxidation appears for both catalysts in the first scan and disappears in the next scan, indicating that the chemisorbed CO is completely oxidized in the first positive potential forward scan. The onset potential and peak potential of the CO oxidation on Pt/Fe-C are 0.54 and 0.64 V respectively and are slightly shifted to negative region compared to that on Pt/C electrode (0.59 and 0.65 V); this indicates that Pt/Fe-C is more active than Pt/C in CO oxidation. Therefore, the surface of Pt nanoparticles supported on Fe-C with low d-band centre value most likely bind CO more weakly, resulting in an increased rate of CO oxidation.

Fig. 9 shows the CV scans of Pt/Fe-C and Pt/C in N_2-staturated 0.5 mol L^{-1} H_2SO_4 + 0.5 mol L^{-1} C_2H_5OH in the potential range from

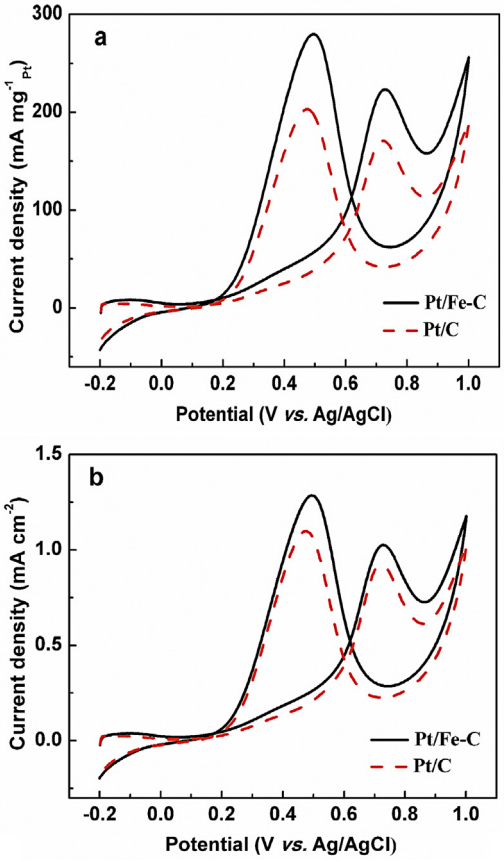

Fig. 9. Cyclic voltammograms for ethanol oxidation on Pt/Fe-C and Pt/C electrodes in N_2-staturated 0.5 mol L^{-1} H_2SO_4 + 0.5 mol L^{-1} C_2H_5OH at a scan rate of 50 mV s^{-1}.

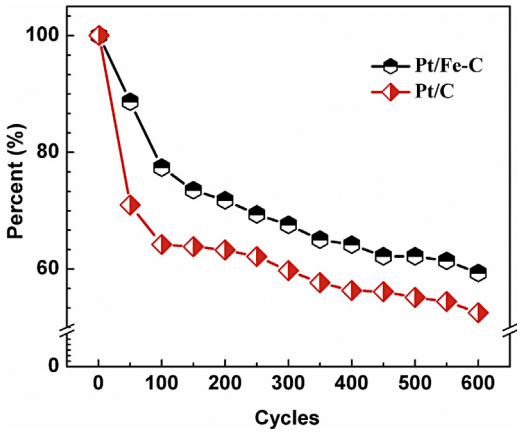

Fig. 10. Peak currents of CV on Pt/Fe-C and Pt/C *vs.* cycle number in 0.5 mol L^{-1} C_2H_5OH + 0.5 mol L^{-1} H_2SO_4.

-0.2 to 1.0 V. The current was normalized to the Pt loading (Fig. 9a) and the *ECSA* (Fig. 9b) respectively. The mass-normalized current is indicative of the catalytic activity per equivalent amount of loaded metal catalysts, and the area-normalized current represents the intrinsic activity of the active sites in the catalyst particles [43]. It can be observed in Fig. 9 that the onset potential on Pt/Fe-C electrode is 0.08 V, negative shift of 32 mV compared to that on Pt/C (0.112 V). Fig. 9a, shows the mass activity of Pt/Fe-C for ethanol oxidation, e.g. the current density of the oxidation peak in the positive scan, which is 224 mA $mg^{-1}{}_{Pt}$ at 0.728 V and higher than that of Pt/C (172 mA $mg^{-1}{}_{Pt}$ at 0.719 V). However, the specific activity of Pt/Fe-C for ethanol oxidation in Fig. 9b reaches 1.03 mA cm^{-2}, which is slightly larger than that of Pt/C at 0.93 mA cm^{-2}. This result indicates that the enhancement in catalytic activity of Pt/Fe-C catalyst is the result of interactions between Pt particles and Fe-C support.

Here, several types of supports are also compared to our results. Zhang et al. [44] reported that SnO_2 flower-like cystal supported Pt particles exhibited the onset potential of 0.1 V *vs.* Ag/AgCl and peak current density of 154.3 mA $mg_{Pt}{}^{-1}$ for ethanol oxidation, indicating that the catalytic activity of their catalyst is poor compared to Pt/Fe-C. When Pt particles supported ordered mesoporous carbon [45], the onset potential of ethanol oxidation on it is at ca. 0.30 V *vs.* RHE, manifesting a positive shift of ca. 20 mV wih respect to that on Fe-C. Pt particles supported on maganese oxide-carbon nanotubes [46] display high catalytic activity for ethanol oxidation, e.g. -0.15 V vs. Hg/Hg_2SO_4 of the onset potential and 1141.4 mA $mg_{Pt}{}^{-1}$ of the forward peak current density, which is better than that of Pt/Fe-C. These results indicate that Fe-C is a promising support in electrocatalysis and the catalytic activity of Pt/Fe-C should be improved in the future work.

For practical PEMFC operation, catalyst stability is very important. This was next evaluated by monitoring the peak current loss with the cycle number (Fig. 10). After 600 cycles, the peak current for ethanol oxidation on Pt/Fe-C was 59.3% relative to the initial peak current. In contrast, the peak current on Pt/C electrode only retains 52.5% of the original value. Therefore, the rate of Pt/C degradation was higher than that of Pt/Fe-C, showing that Pt/Fe-C is more stable than Pt/C due to the strong interaction between Pt nanoparticles and Fe/C.

4. Conclusions

An iron nanoparticle-inserted carbon nanotube/graphite composite was synthesized and evaluated as a support for a Pt nanoparticle PEMFC anode catalyst. Compared to Vulcan carbon, its unique morphology and N-containing active surface sites enable Fe-C to support a high (40 wt%) loading of Pt nanoparticles with small particle size and uniform dispersion. Pt/Fe-C catalyst had enhanced catalytic activity for ethanol oxidation compared to Pt/C (40 wt%). Furthermore, Pt/Fe-C had greater stability in EOR than Pt/C due to the strong interaction between Pt nanoparticles and Fe-C support. Therefore, the Fe-C support provides a promising model for the preparation of other high loading Pt-based alloy fuel cell catalysts.

Acknowledgment

The authors would like to thank the National Natural Science Foundation of China (21163018, 21363022, and 51362027) for financially supporting this work.

Appendix A. Supplementary data

Supplementary data associated with this article can be found, in the online version, at http://dx.doi.org/10.1016/j.electacta.2014.03.153.

References

[1] R. Bashyam, P. Zelenay, Nature 443 (2006) 63–66.
[2] C.W. Bezerra, L. Zhang, K. Lee, H. Liu, A.L. Marques, E.P. Marques, H. Wang, J. Zhang, Electrochimica Acta 53 (2008) 4937–4951.
[3] H. Wang, V. Linkov, S. Ji, W. Zhang, Z. Lei, R. Wang, South African Journal of Chemistry 65 (2012) 69–74.
[4] F. Su, Z. Tian, C.K. Poh, Z. Wang, S.H. Lim, Z. Liu, J. Lin, Chemistry of Materials 22 (2009) 832–839.
[5] J. Ribeiro, D.M. dos Anjos, K.B. Kokoh, C. Coutanceau, J.M. Léger, P. Olivi, A.R. de Andrade, G. Tremiliosi-Filho, Electrochimica Acta 52 (2007) 6997–7006.
[6] B. Lim, M. Jiang, P.H. Camargo, E.C. Cho, J. Tao, X. Lu, Y. Zhu, Y. Xia, Science 324 (2009) 1302–1305.
[7] E. Proietti, F. Jaouen, M. Lefèvre, N. Larouche, J. Tian, J. Herranz, J.-P. Dodelet, Nature Commnunications 2 (2011) 416.
[8] Y. Bing, H. Liu, L. Zhang, D. Ghosh, J. Zhang, Chemistry Society Reviews 39 (2010) 2184–2202.
[9] R. Wang, K. Wang, H. Wang, Q. Wang, J. Key, V. Linkov, S. Ji, International Journal of Hydrogen Energy 38 (2013) 5783–5788.
[10] E. Antolini, Applied Catalysis B: Environmental 88 (2009) 1–24.
[11] Y.-J. Wang, D.P. Wilkinson, J. Zhang, Chemical Reviews 111 (2011) 7625–7651.
[12] Y. Chen, J. Wang, H. Liu, M.N. Banis, R. Li, X. Sun, T.-K. Sham, S. Ye, S. Knights, The Journal of Physical Chemistry C 115 (2011) 3769–3776.
[13] C.L. Sun, Y.K. Hsu, Y.G. Lin, K.H. Chen, C. Bock, B. MacDougall, X.H. Wu, L.C. Chen, Journal of The Electrochemical Society 156 (2009) B1249–B1252.
[14] B.P. Vinayan, R. Nagar, N. Rajalakshmi, S. Ramaprabhu, Advanced Functional Materials 22 (2012) 3519–3526.
[15] G. Wu, R. Swaidan, D. Li, N. Li, Electrochimica Acta 53 (2008) 7622–7629.
[16] Y. Jiang, J. Zhang, Y.-H. Qin, D.-F. Niu, X.-S. Zhang, L. Niu, X.-G. Zhou, T.-H. Lu, W.-K. Yuan, Journal of Power Sources 196 (2011) 9356–9360.
[17] W. Sheng, S. Chen, E. Vescovo, Y. Shao-Horn, Journal of the Electrochemical Society 159 (2011) B96–B103.
[18] Y. Ma, S. Jiang, G. Jian, H. Tao, L. Yu, X. Wang, X. Wang, J. Zhu, Z. Hu, Y. Chen, Energy & Environmental Science 2 (2009) 224–229.
[19] C. Roth, M. Goetz, H. Fuess, Journal of Applied Electrochemistry 31 (2001) 793–798.
[20] R. Wang, X. Li, H. Li, Q. Wang, H. Wang, W. Wang, J. Kang, Y. Chang, Z. Lei, International Journal of Hydrogen Energy 36 (2011) 5775–5781.
[21] R. Wang, T. Zhou, X. Qiu, H. Wang, Q. Wang, H. Feng, V. Linkov, S. Ji, International Journal of Hydrogen Energy 38 (2013) 10381–10388.
[22] J.C. Jia, R.F. Wang, H. Wang, S. Ji, J. Key, V. Linkov, K. Shi, Z.Q. Lei, Catalysis Communications 16 (2011) 60–63.
[23] R. Wang, J. Jia, H. Wang, Q. Wang, S. Ji, Z. Tian, Journal Solid State Electrochemistry 17 (2013) 1021–1028.
[24] S. Sun, G. Zhang, D. Geng, Y. Chen, M.N. Banis, R. Li, M. Cai, X. Sun, Chemistry–A European Journal 16 (2010) 829–835.
[25] D. Deng, L. Yu, X. Chen, G. Wang, L. Jin, X. Pan, J. Deng, G. Sun, X. Bao, Angewandte Chemie International Edition 52 (2013) 371–375.
[26] B. Fang, J.H. Kim, M. Kim, J.S. Yu, Physical Chemistry Chemical Physics 11 (2009) 1380–1387.
[27] B. Fang, J.H. Kim, M. Kim, J.-S. Yu, Chemistry of Materials 21 (2009) 789–796.
[28] V. Di Noto, E. Negro, Electrochimica Acta 55 (2010) 7564–7574.
[29] Z. Chen, D. Higgins, H. Tao, R.S. Hsu, Z. Chen, The Journal of Physical Chemistry C 113 (2009) 21008–21013.
[30] C.H. Choi, S.H. Park, S.I. Woo, International Journal of Hydrogen Energy 37 (2012) 4563–4570.

[31] J.R. Pels, F. Kapteijn, J.A. Moulijn, Q. Zhu, K.M. Thomas, Carbon 33 (1995) 1641–1653.
[32] D.-J. Guo, L. Zhao, X.-P. Qiu, L.-Q. Chen, W.-T. Zhu, Journal of Power Sources 177 (2008) 334–338.
[33] H. Xiao, Z.-G. Shao, G. Zhang, Y. Gao, W. Lu, B. Yi, Carbon 57 (2013) 443–451.
[34] H. Peng, Z. Mo, S. Liao, H. Liang, L. Yang, F. Luo, H. Song, Y. Zhong, B. Zhang, Scientific Reports 3 (2013) 1765.
[35] K. Ai, Y. Liu, C. Ruan, L. Lu, G.M. Lu, Advanced Materials 25 (2013) 998–1003.
[36] K.L. Wang, H. Wang, S. Pasupathi, V. Linkov, S. Ji, R.F. Wang, Electrochimica Acta 70 (2012) 394–401.
[37] H. Wang, R. Luo, S. Liao, J. Key, S. Ji, R. Wang, Journal Solid State Electrochemistry 17 (2013) 2009–2015.
[38] D. He, Y. Jiang, H. Lv, M. Pan, S. Mu, Applied Catalysis B: Enviromental 132–133 (2013) 379–388.
[39] T. Zhou, H. Wang, K. Julian, S. Ji, V. Linkov, R. Wang, RSC Advances 3 (2013) 16949–16953.
[40] G. Bae, D.H. Youn, S. Han, J.S. Lee, Carbon 51 (2013) 274–281.
[41] X.T. Zhang, H. Wang, J. Key, V. Linkov, S. Ji, X.L. Wang, Z.Q. Lei, R.F. Wang, Journal of The Electrochemical Society 159 (2012) B270–B276.
[42] H. Wang, Z. Liu, S. Ji, K. Wang, T. Zhou, R. Wang, Electrochimica Acta 108 (2013) 833–840.
[43] J.M. Lee, S.B. Han, J.Y. Kim, Y.W. Lee, A.R. Ko, B. Roh, I. Hwang, K.W. Park, Carbon 48 (2010) 2290–2296.
[44] H. Zhang, C. Hu, X. He, L. Hong, G. Du, Y. Zhang, Journal of Power Source 196 (2011) 4499–4505.
[45] M.H. Chen, Y.X. Jiang, S.R. Chen, R. Huang, J.L. Lin, S.P. Chen, S.G. Sun, The Journal of Physical Chemistry C 114 (2010) 19055–19061.
[46] J. Cai, Y. Huang, B. Huang, S. Zheng, Y. Guo, International Journal of Hydrogen Energy 39 (2014) 798–807.